Hierarchically Porous CuO Hollow Spheres Fabricated via a One-Pot Template-Free Method for High-Performance Gas Sensors

Yao Qin,[†,‡] Feng Zhang,[‡] Yun Chen,[‡] Yanjie Zhou,[†] Jie Li,[†] Anwei Zhu,[‡] Yongping Luo,[‡] Yang Tian,*[,†,‡] and Jinhu Yang*[,†,‡,§]

[†]Institute for Advanced Materials and Nano Biomedicine, and [‡]Department of Chemistry, Tongji University, Siping Road 1239, Shanghai 200092, People's Republic of China

[§]Key Laboratory for Ultrafine Materials of Ministry of Education, School of Materials Science and Engineering, East China University of Science and Technology, Shanghai 200237, China

Ⓢ *Supporting Information*

ABSTRACT: CuO hollow spheres with hierarchical pores, that is, quasi-micropores (1.0−2.2 nm), mesopores (5−30 nm), and macropores (hollow cores, 2−4 μm), have been synthesized via a simple one-pot template-free method. The CuO hollow spheres also show a hierarchical architecture, namely, the primary CuO nanograins, the quasi-single-crystal nanosheets assembled by nanograins, and the spheres composed of the nanosheets. A mechanism involving an "oriented attachment" growth step followed by an "Ostwald ripening" process has been proposed for the hierarchical structure and pore formation of the typical CuO hollow spheres. With such unique hierarchical pores and architecture, the CuO hollow spheres display excellent sensing performance toward H_2S as gas sensing material, such as low detection limit of 2 ppb, high sensitivity at parts per billion level concentration, broad linear range, short response time of 3 s, and recovery time of 9 s. The excellent performance is ascribed to a synergetic effect of the hierarchical structure of the unique CuO spheres: the quasi-micropores offer active sites for effectively sensing, the mesopores facilitate the molecular diffusion kinetics, and the macropores serve as gas reservoirs and minimize diffusion length, while good conductivity of the quasi-single-crystal nanosheets favors fast charge transportation, which contribute to the high sensitivity, quick response, and recovery of the H_2S sensor, respectively.
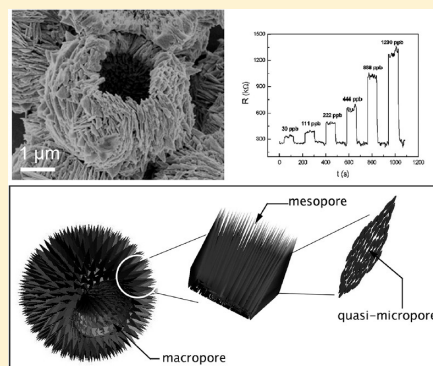
INTRODUCTION

Hierarchical hollow or porous structures have attracted great interest because of their important applications in photocatalysis, drug delivery, nanoreactors, energy conversion and storage systems, photonic devices, and chemical sensors.[1−9] As a unique micro/nanostructure, hollow spheres are considered to be desirable as gas sensing materials due to their less gas diffusion length and relatively larger specific surface area than agglomerated nanoparticles as well as higher mobility for easy and stable sensing film assembly.[9−14] However, hollow spheres often suffer from problems of limited active sites and poor diffusion. For example, when the shells of hollow spheres are very thick or compact, the inward diffusion of analyte gas is greatly hampered, and the inner sensing reaction just happens near the surface region of the hollow spheres, which makes the inner part of the hollow sphere inactive and leads to a low gas response.[15] In this regard, gas-permeable porous shells contain mesopores and micropores that allow the gas diffusion toward the entire sensing surface are highly desired. To date, the hollow spheres with either mesoporous or microporous shells have been prepared by templating methods with high-temperature heating treatment,[16] but few of them obtain well-defined mesopores and micropores simultaneously. In fact, from the viewpoint of sensing, both mesopores and micropores

are very necessary for hollow spheres, as they can serve as effective transport channels and active sensing sites for analyte gas molecules, which are crucial for high sensitivity and quick response.[17] However, fabrication of hollow spheres with well-defined hierarchical pores and structure remains a great challenge, especially, via a facile one-pot template-free approach and with high sensing performance.

As one of the most toxic and flammable gases, H_2S affects the nervous system of humans and can cause people to lose consciousness at very low concentrations. The acceptable levels of H_2S in the ambient environment (recommended by the Scientific Advisory Board on Toxic Air Pollutants, USA) are reported to be within the range 20−100 ppb.[18] So far, lots of metal oxide materials have been employed for H_2S detection, such as SnO_2, ZnO, WO_3, and so on.[19−22] Unfortunately, most of these works showed that the H_2S sensor responses as a function of gas concentrations are in the range 10−50 ppm at relatively high temperatures. Therefore, it is imperative that more special efforts need be paid on exploring novel sensing materials with a parts per billion level detection limit and high
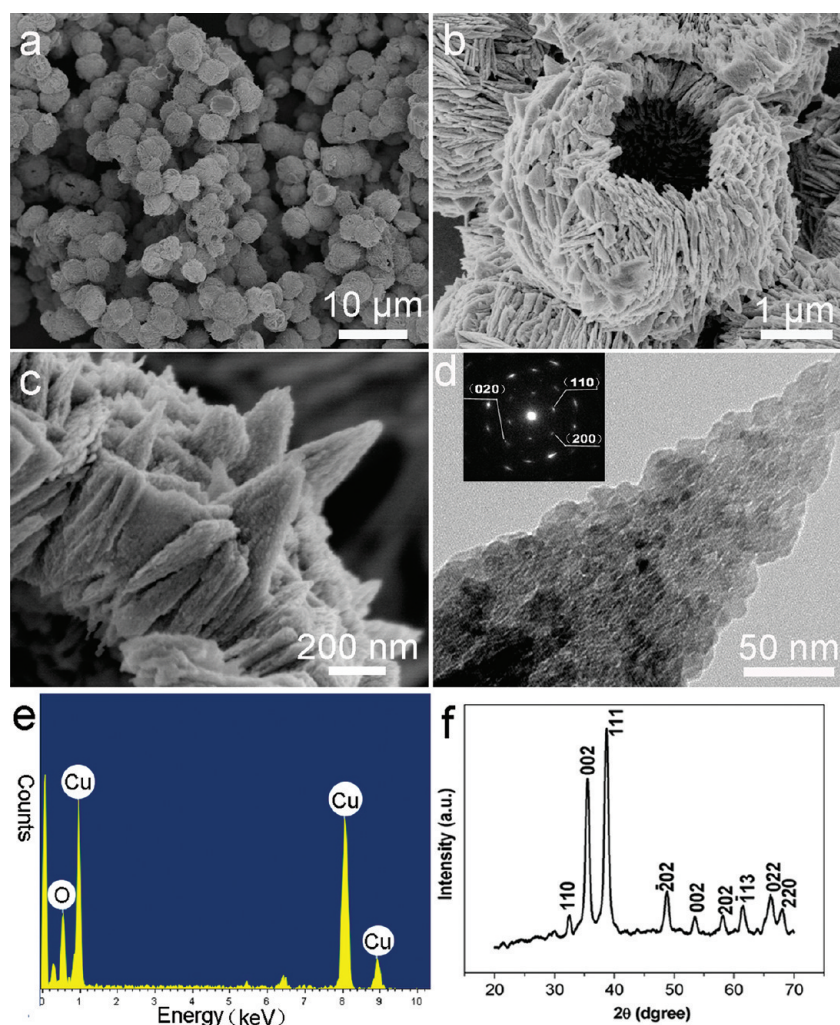
Figure 1. (a−c) SEM and (d) TEM images, (e) EDS spectrum, and (f) XRD pattern of the hierarchically porous CuO spheres with the incubation time of 24 h. (a) Low-magnification image and (b) high-magnification image of an individual CuO sphere; (c) high-magnification image showing the wall structure of CuO spheres; (d) TEM image of a typical nanosheet fell from the CuO spheres. Inset of (d) is ED pattern of the nanosheet tip.

sensitivity. Copper oxide (CuO) is one of the few metal oxides that show both p-type semiconducting property and strong affinity toward H_2S.[23] Many interesting structures including hierarchical CuO hollow spheres[24−29] have been prepared. In our recent work, leafletlike CuO nanosheets have been synthesized with an ease-to-preparation and environmentally friendly method and first developed for sensitive and selective detection of H_2S.[30]

In this context, we report a simple one-pot template-free method for synthesis of CuO hollow spheres with hierarchical pores and structure by merely using $CuSO_4$, KOH, and $NH_3 \cdot H_2O$ aqueous solution at 68 °C. The CuO hollow spheres have a novel three-order hierarchical architecture, namely, the primary CuO nanograins, the spindlelike quasi-single-crystal nanosheets assembled by nanograins, and the hollow spherical shell composed of spindlelike nanosheets. Moreover, the hierarchical CuO hollow spheres exhibit three kinds of hierarchical pores, that is, quasi-micropores (1.0−2.2 nm), mesopores (5−30 nm), and macropores (hollow cores, 2−4 μm). A mechanism involving an "oriented attachment" growth step of nanograins followed by an "Ostwald ripening" process has been proposed for the hierarchical structure and pore formation. As expected, the hierarchically porous CuO spheres show enhanced sensing performance toward H_2S, for example,

lower detection limit, higher sensitivity, quicker response, and shorter recovery time at even lower working temperature, compared with nanomaterial-based H_2S sensors reported previously. The remarkable analytical performance may be attributed to a synergistic effect of the unique structure of the CuO hollow spheres.

■ EXPERIMENTAL SECTION

Materials. $CuSO_4 \cdot 5H_2O$, KOH, and concentrated ammonia ($NH_3 \cdot H_2O$) were purchased from Shanghai Chemical Reagent Co. Ltd. and used as supplied. The H_2S gas was purchased from Shanghai Shenkai Gases Technology Co. Ltd. O_2 and N_2 were obtained from Shanghai Chunyu Specialty Gases Co. Ltd. Other reagents were of analytical grade and used as purchased.

Synthesis of the Hierarchically Porous CuO Hollow Spheres. In a typical experiment, 3 mL of $CuSO_4$ solution (0.4 M), 1 mL of KOH solution (0.48 M), and 0.9 mL of commercial ammonia were mixed together, followed by addition of 15 mL of distilled water under constant stirring to form a homogeneous, transparent dark blue solution. The mixture was then transferred into a water bath at 68 °C and incubated for a different time. The resulting black precipitate was centrifuged and washed with distilled water for four

11995

dx.doi.org/10.1021/jp212029n | J. Phys. Chem. C 2012, 116, 11994−12000

times. The product was redispersed in distilled water for further characterizations.

Characterization. Morphology was characterized using a scanning electron microscope (SEM, Hitachi S4800, 3 kV) and high-resolution transmission electron microscopy (HR-TEM, JEM 2011, 200 kV) together with associated energy-dispersive X-ray spectroscopy (EDS). X-ray photoelectron spectroscopy (XPS) investigation was conducted in PHI-5000C ESCA system (Perkin−Elmer) with Mg Kα radiation ($h\nu$ = 1253.6 eV). The XPS spectra of the studied elements were measured with a constant analyzer pass energy of 46.95 eV. All binding energies (BEs) were referred to the C 1s peak (284.6 eV) arising from surface hydrocarbons (or adventitious hydrocarbon). The crystal structure was determined by X-ray diffraction (XRD) using a D/max2550VB3+/PC X-ray diffractometer with Cu Kα radiation with a 1.5418 Å wavelength. A beam voltage of 40 kV and a 100 mA current beam were used.

H$_2$S Gas Sensing Performance Evaluation. The electrical and gas sensing properties of the synthesized CuO solid and hollow spheres were measured with a WS-30A system (Zhengzhou Winsen Electronics Technology Co. Ltd., China), equipped with a stainless steel chamber and a temperature controlled chuck. The as-prepared CuO products were mixed with deionized water and coated on an alumina tubelike substrate, on which a pair of Au electrodes with a gap of ~1.5 mm had been printed at the two ends. Then, the CuO-coated substrate was dried at 80 °C for ~5 min and subsequently annealed at 500 °C for ~1 h. Finally, a Ni−Cr alloy coil was inserted into the tube as a heater, which provided the working temperature of the gas sensor. Before measurements, the chamber was kept under a continuous flow of fresh air for 30 min. A given amount of H$_2$S was injected into the chamber by a microsyringe. The sensor response was defined as $100(R_g - R_a)/R_a$, where R_a and R_g are the electrical resistances for sensors in air and in H$_2$S, respectively. The response time is defined as the time required for the variation in conductance to reach 90% of the equilibrium value after H$_2$S was injected and the recovery time as the time necessary for the sensor to return to 10% above the original conductance in air after releasing H$_2$S.

■ RESULTS AND DISCUSSION

The scanning electron microscopy (SEM) images of the as-synthesized CuO spheres are given in Figure 1. From low-magnification images in Figure 1a, we can see that the CuO products are mainly composed of uniform spheres with diameters of ~3−5 μm in very high yield. Magnified images of a crashed CuO sphere (Figure 1b) demonstrate that the CuO sphere has a hollow interior with a wall thickness of ~500 nm. The high-resolution SEM image in Figure 1c shows that the sphere wall consists of many spindlelike nanosheets with average width of ~250 nm and thickness of ~50 nm. Furthermore, a closer observation reveals that the spindlelike nanosheets are composed of even smaller grain particles. Accordingly, the delicate CuO sphere with birdnest appearance has three-order hierarchical structures: small grain particles → spindlelike nanosheets of grain aggregation → hollow spheres of nanosheet assembly.

The detailed structures of the CuO spheres were further investigated by transmission electron microscopy (TEM) as shown in Figure 1d and Figure S1 of the Supporting Information. After fierce ultrasonic treatment, the spindlelike nanosheet fell down from the shell of the CuO sphere was

observed in the TEM sample. A magnified image of one nanosheet tip in Figure 1d reveals that the spindlelike nanosheet actually is composed of even smaller spindlelike nanograins with a diameter of ~3 nm and a length of ~10 nm, which conforms well to the SEM result in Figure 1c. These nanograins tend to align along a preferential direction of [010] (according to the indexed selected area electron diffraction pattern inserted in Figure 1d). Due to self-aggregation of nanograins, abundant slitlike quasi-micropores (estimated to be 1−2.5 nm) are formed in the spindlelike nanosheets. This observation is analogous to that reported by Zeng's and Qi's groups,[24,31] where the slits in the leaflike nanosheets were formed by aggregation of CuO nanostrips aligning along a preferential direction of [010]. The inset of the electron diffraction (ED) pattern in Figure 1d taken from the nanosheet tip shows a set of spots associated with the [001] zone axis of monoclinic CuO. The slightly elongated spots in the pattern also elucidate that the spindlelike nanosheets were formed via an "oriented attachment" process[32] and took a quasi-single-crystalline character. The EDS spectrum of the spindlelike nanosheets supported by a nickle grid is shown in Figure 1e. Only Cu and O signals appear in the spectrum with a Cu/O atom ratio of 50.14:49.86, indicating the composition of the nanosheets is pure CuO. The corresponding X-ray diffraction (XRD) pattern confirms (Figure 1f) the pure CuO formation with monoclinic symmetry (JCPDS card no. 41-0254) and a good crystallinity. The broadening of the recorded peaks indicates that size of the primary component crystallites is at the nanometer scale. This is also evidence of the "oriented attachment" mechanism that the spindlelike sheets were formed via ordered self-organization of the primary nanograins. In addition, in X-ray photoelectron spectroscopy (XPS) analysis (Supporting Information, Figure S2), the typical Cu $2p^{3/_2}$ peak with a measured binding energy of ~934.2 eV as well as its concomitant shakeup line at ~942.4 eV indicates the paramagnetic chemical state of Cu^{2+}.[33] Meanwhile, the well-resolved O$_{1s}$ peak is observed at ~532.6 eV, confirming the chemical composition of the as-prepared products is CuO.

The BET measurement in Figure 2 reveals clearly the hierarchically porous character of the CuO spheres. Two
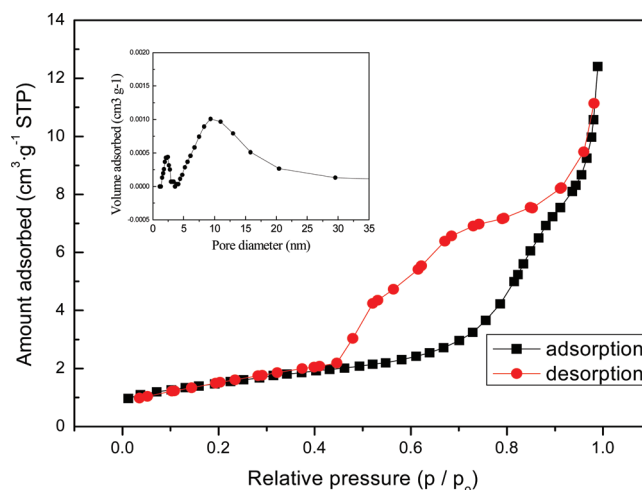

Figure 2. Nitrogen adsorption−desorption isotherm of the hierarchically porous CuO spheres with an incubation time of 24 h. The inset shows the corresponding pore size distribution obtained from the adsorption curve.

regions of pore size distribution (Figure 2, inset), 1.0−2.2 nm and 5−30 nm, identify the presence of the quasi-micropores with a narrow distribution and the mesopores with a wide distribution. The quasi-micropores agree well with the slitlike pores observed in spindlelike nanosheets resulted from the nanograin attachment, and the mesopores can be reasonably ascribed to the self-assembly of the nanosheets (50−250 nm) during which internanosheet mesopores could be produced. Therefore, plus the hollow cores (macropores), the CuO spheres possess hierarchical pores, that is, quasi-micropores (1.0−2.2 nm), mesopores (5−30 nm), and macropores (2−4 μm). As far as we know, this is the first time that the CuO hollow spheres with hierarchical structure and pores have been reported via a one-pot template-free method.

To explore the formation mechanism of the hierarchical structure and pores, the CuO products obtained at different reaction stages during the growth process were also investigated. SEM images of CuO products obtained at different growth times were given in Figure 3. It was found
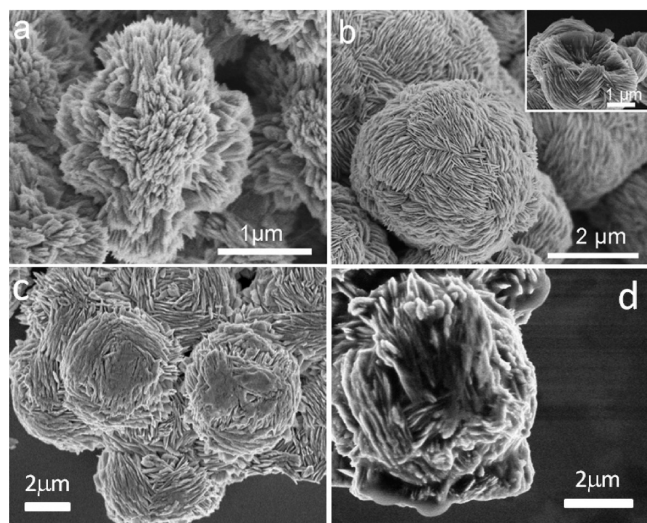

Figure 3. SEM images of CuO products obtained at different growth times: (a) 0.5 h, (b) 1 h, and (c, d) 10 h. (d) and inset in (b) are the crushed CuO spheres.

that large amounts of CuO bundles with rough surfaces consisted of spindlelike nanosheets were initially formed at a reaction time of 0.5 h (Figure 3a). Subsequently, driven by the reactants at high concentration, these CuO bundles grew up
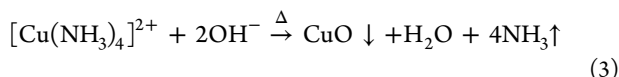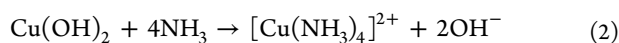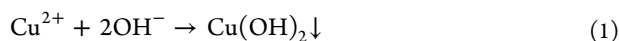
rapidly into well-defined micorspheres (~3 μm) at an earlier stage of 1 h by assembly of more nanosheets (Figure 3b) and then slowly into larger spheres (~4 μm) at 10 h (Figure 3c). The assembly of the nanosheets led to mesopore formation between the nanosheets and is evidenced by BET characterization of the spheres shown in Figure 2. A crushed CuO sphere by ultrasonic treatment (Figure 3b, inset) at 1 h shows a solid core. Another crushed sphere obtained at 10 h also displays a basically solid core, but in contrast, the core seems to be getting looser (Figure 3d), indicating a slow core-hollowing process is proceeding. In fact, we did not find apparent hollowing of these spheres until the reaction time was prolonged to 20 h. The time effect reveals an "Ostwald ripening" mechanism for the hollowing process of the CuO spheres, as it is well-known that during "Ostwald ripening" process crystallites grow at expense of smaller ones, leading to cavity formation and accordingly, crystallinity increase.[34,35] This is well mirrored in the XRD results of the samples (Supporting Information, Figure S3), that is, the crystallinity of CuO products prepared with a reaction time of 24 h is obviously increased after the hollowing process, compared with that of 1 h.

The ratio of $[Cu^{2+}]/[OH^-]/[NH_3\cdot H_2O]$ in the preparation was optimized to be ~5:2:100. At this high concentration ratio of NH_3, no $Cu(OH)_2$ precipitation was produced. The transparent precursor solution shows a dark blue color, which is ascribed to the existence of $[Cu(NH_3)_4]^{2+}$ according to reactions 1 and 2. It is noteworthy that, in many reports, CuO nanostructures were formed through decomposition of Cu-$(OH)_2$ precursor (reaction 4).[31,36] But in our work, most probably a direct transformation of $[Cu(NH_3)_4]^{2+}$ precursor ions to CuO primary nanograins occurred according to reaction 3. As shown in Scheme 1, a two-step mechanism is proposed here for the formation process of the CuO spheres with the hierarchical structure and pores: (1) the "oriented attachment" growth step. It is reasonable that the nucleation of CuO started from localized regions where concentrations of OH^- and $[Cu(NH_3)_4]^{2+}$ are relatively high. Around the preformed nuclei center, a large number of primary CuO nanograins were produced. Subsequently, the fast oriented attachment of these CuO nanograins resulted in the formation of CuO nanosheet bundles, simultaneously, the formation of quasi-micropores as well. Driven by surface energy minimization, the nanosheet bundles gradually assembled into the spherical shape CuO assemblies, accompanied by the mesopore generation. (2) The "Ostwald ripening" step. Compared to those in the outer

Scheme 1. Schematic Illustration for the Formation Process of the Hierarchical Structure and Pores of the CuO Spheres
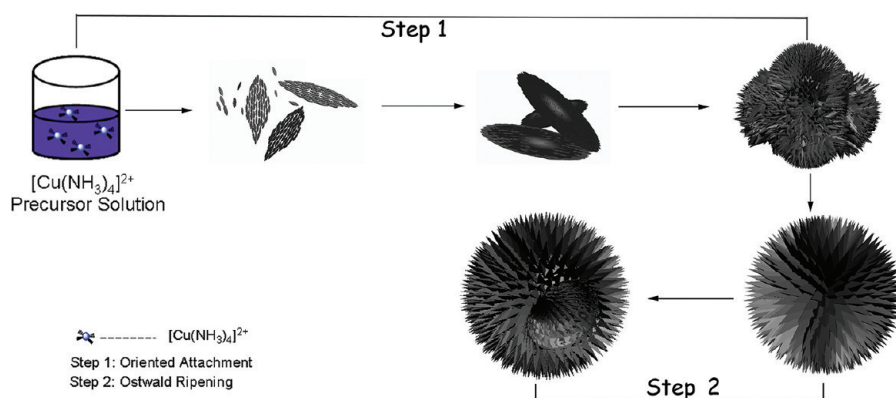
surfaces, the CuO crystallites located in the inner cores have relatively high surface energies possibly due to the defects of mismatch generated from the high growth rate at the early "oriented attachment" stage. On the other hand, as mentioned in Liu's work,[24] the inner cores can be visualized as a smaller sphere having a higher curvature. Thus, they are prone to dissolving during the incubation process. With the reaction time prolonging, the unstable inner cores dissolved gradually, and the macropores were formed in the CuO spheres.

$$Cu^{2+} + 2OH^- \rightarrow Cu(OH)_2\downarrow \tag{1}$$

$$Cu(OH)_2 + 4NH_3 \rightarrow [Cu(NH_3)_4]^{2+} + 2OH^- \tag{2}$$

$$[Cu(NH_3)_4]^{2+} + 2OH^- \xrightarrow{\Delta} CuO\downarrow + H_2O + 4NH_3\uparrow \tag{3}$$

$$Cu(OH)_2 \rightarrow CuO + H_2O \tag{4}$$

To demonstrate the potential application of the as-prepared hierarchically porous CuO spheres in a gas sensor, we examined the analytical performance toward H_2S based on the present CuO spheres. As shown in Figure 4A, the sensor resistance
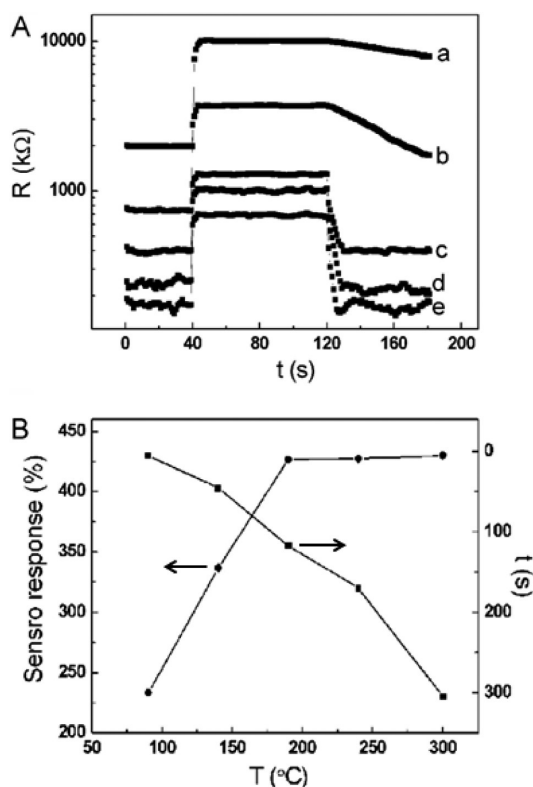
Figure 4. (A) Change in electrical resistance obtained at the hierarchically porous CuO spheres toward 1 ppm H_2S at (a) 90 °C, (b) 140 °C, (c) 190 °C, (d) 240 °C, and (e) 300 °C working temperatures. (B) Plot of response and recovery time versus working temperature obtained at the hierarchically porous CuO spheres toward 1 ppm H_2S.

increased sharply upon exposure to H_2S and then decreased to the initial resistance when the chamber was purged with dry air. From this figure, it is clear that the change in electrical resistance, as well as the recovery time, is strongly dependent on the working temperature applied at the substrates. As plotted in Figure 4B, the sensor response increased with the

increasing working temperature up to 190 °C and then decreased, while the recovery time shortened with the increasing working temperature as expected, and reached the minimum value of ~9 s at 190 °C. By taking into account the sensor response, recovery time, and temperature, the optimized working temperature was selected as 190 °C. Figure 5 presents
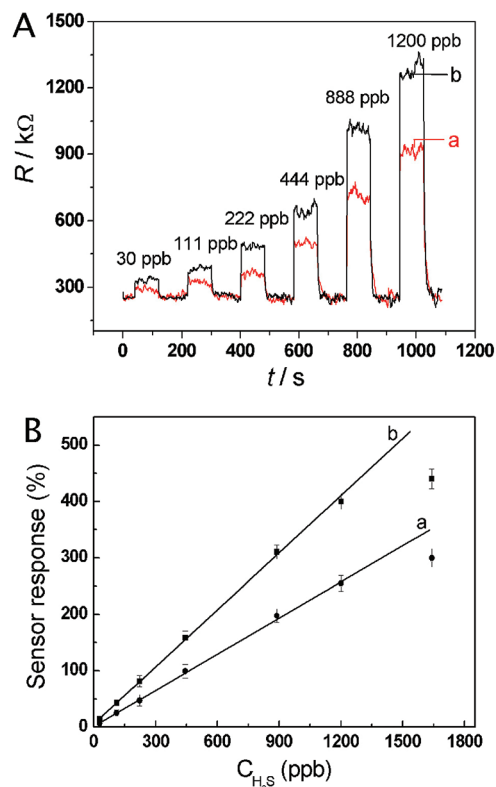
Figure 5. (A) Changes in electrical resistance toward different concentrations of H_2S at the working temperature of 190 °C obtained at (a) the porous CuO spheres with small nanopores (<4 nm) and (b) the hierarchically porous CuO spheres. (B) Calibration curves of sensor response versus H_2S concentration at the working temperature of 190 °C based on (a) the solid CuO spheres and (b) the hierarchically porous CuO spheres.

the sensing performance toward H_2S based on the two type CuO spheres obtained at the different reaction times of 24 and 1 h, that is, the hollow spheres with hierarchical pores and the porous spheres with small nanopores (<4 nm) (Figure 3b and Figure S4 of the Supporting Information). As expected, the increase in the sensor resistance is in proportion to the concentration of H_2S. Although both types of CuO spheres can provide very good capability, the typical CuO hollow spheres are apparently even better. Moreover, the sensor fabricated from the hierarchically porous CuO spheres have shown a lower detection limit of 2 ppb, a broader dynamic linear range from 30 to 1350 ppb, higher sensitivity, and shorter response time of 3 s, and recovery time of 9 s for H_2S sensing, compared with those obtained by solid CuO structures, CuO nanowires, and other reported works using Pt−In_2O_3 nanocomposites, In_2O_3 whisker.[36−39] In addition, the gas responses toward other gases that may exist in the atmosphere were examined using the hierarchically porous CuO spheres. The gas responses toward 100 ppm H_2, NH_3, O_2, CO, CH_4, and N_2 were much lower, even compared with that to 1 ppm H_2S (Figure 6). This

observation indicates the high selectivity of the present H_2S gas sensor based on the typical CuO spheres.
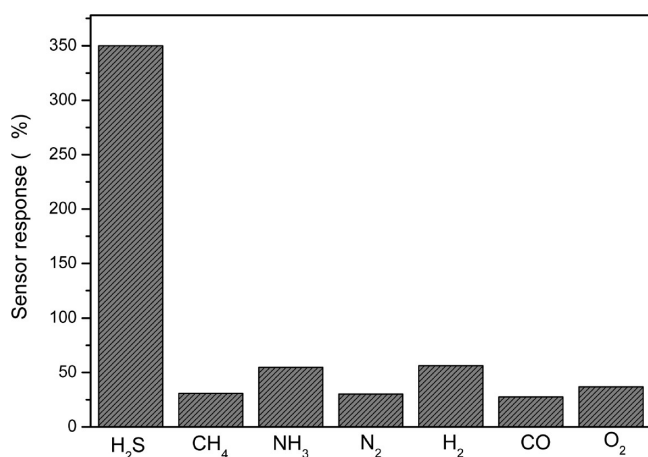
Figure 6. Sensor responses obtained for the hierarchically porous CuO spheres at the working temperature toward 1 ppm H_2S and 100 ppm CH_4, NH_3, N_2, H_2, CO, and O_2.

The operating principles of p-type transition metal oxide chemiresistor gas sensors are based on change of sensor conductivity by controlling mobile charge carriers. When the p-type CuO is exposed to H_2S, electrons from the redox reactions between H_2S and adsorbed surface oxygen will be injected to the conduction band of CuO, and the recombination between the electrons and holes will result in a lower carrier concentration. Subsequently, the negative quasi-gate voltage is reduced, and in turn, the resistance of CuO increases. The significant variation in resistance can be attributed to the special structure advantages of the hierarchically porous CuO spheres. The abundant quasi-micropores in the spindlelike nanosheets that compose the CuO shells endow the material a large quantity of active sites for H_2S sensing, which is considered to be one of the key roles for low detection limit and enhanced sensitivity. The mesopores provide direct diffusion channels and facilitate H_2S molecule diffusion kinetics and fast adsorption/desorption on the interface, while the macropores work as H_2S molecule-buffering reservoirs and minimize distance to the mesoporous channels; in addition, good conductivity of the quasi-single-crystal nanosheets may allow higher charge transportation during the sensing process, with all of these being responsible for quick response and short recovery time of the H_2S sensor. It is noteworthy that carbon materials with similar hierarchical pores display superior performance in energy storage.[9] Therefore, with these merits, the hierarchically porous CuO hollow spheres may find more applications in related fields such as photocatalysis, solar cells, lithium batteries, and electrochemical capacitors.

CONCLUSIONS

In summary, we have successfully fabricated the CuO hollow spheres with hierarchical architecture and pores via a simple one-pot template-free method. The growth mechanism of "oriented attachment" followed by "Ostwald ripening" has been proposed to explain the formation of the hierarchical structure and pores of the CuO spheres. In brief, the quasi-micropores and the mesopores are formed by the primary nanograin attachment and the nanosheet assembly, respectively, while the macropores (hollow interior) of the CuO spheres are produced by self-hollowing driven by the "Ostwald ripening" process. The unique CuO spheres exhibited excellent sensing performance, such as low detection limit, high sensitivity, and quick response and recovery time, due to the special structure with open macropores for gas molecule buffering, mesopores and micropores for fast H_2S molecule diffusion and effectively sensing, and good conductivity of the quasi-single-crystal nanosheets for fast carrier transportation. This investigation provides an effective, facile, and green methodology for synthesizing metal oxide materials with hierarchical architecture and pores. The typical CuO spheres are also promising in other oxide semiconductor-related fields where diffusion kinetics and interface property play decisive roles, such as solar cells, lithium batteries, photocatalysis, and so on. The related investigations are under way.

■ ASSOCIATED CONTENT

Ⓢ Supporting Information

High-magnification TEM image (Figure S1), X-ray photoelectron spectra (Figure S2), XRD patterns at different reaction time (Figure S3), and pore distribution curve (Figure S4) of the CuO spheres. This material is available free of charge via the Internet at http://pubs.acs.org.

■ AUTHOR INFORMATION

Corresponding Author

*E-mail: (J. Y.) yangjinhu2010@gmail.com; (T. Y.) yangtian@tongji.edu.cn. Fax: (J. Y.) 86-021-65983706. Phone: (J. Y.) 86-021-65988029.

Notes

The authors declare no competing financial interest.

■ ACKNOWLEDGMENTS

■ REFERENCES

(1) Lu, A. H.; Li, W. C.; Hao, G. P.; Spliethoff, B.; Bongard, H. J.; Schaack, B. B.; Schuth, F. *Angew. Chem., Int. Ed.* **2010**, *49*, 1615−1618.

(2) Wang, L. Z.; Tang, F. Q.; Ozawa, K.; Chen, Z. G.; Mukherj, A.; Zhu, Y. C.; Zou, J.; Cheng, H. M.; Lu, G. Q. *Angew. Chem., Int. Ed.* **2009**, *48*, 7048−7051.

(3) Walsh, D.; Mann, S. *Nature* **1995**, *377*, 320−323.

(4) Benabid, F.; Couny, F.; Knight, J. C.; Birks, T. A.; Russell, P. S. *Nature* **2005**, *434*, 488−491.

(5) An, K.; Hyeon, T. *Nano Today* **2009**, *4*, 359−373.

(6) Wei, W.; Ma, G. H.; Hu, G.; Yu, D.; McLeish, T.; Su, Z. G.; Shen, Z. Y. *J. Am. Chem. Soc.* **2008**, *130*, 15808−15810.

(7) (a) Wang, D. W.; Li, F.; Liu, M.; Lu, G. Q.; Cheng, H. M. *Angew. Chem., Int. Ed.* **2008**, *47*, 373−376. (b) Qiu, Y. F.; Yang, S. H. *Adv. Funct. Mater.* **2007**, *17*, 1345−1352.

(8) Liu, J.; Qiao, S. Z.; Hartono, S. B.; Lu, G. Q. *Angew. Chem., Int. Ed.* **2010**, *49*, 4981−4985.

(9) Lai, X. Y.; Li, J.; Korgel, B. A.; Dong, Z. H.; Li, Z. M.; Su, F. B.; Du, J.; Wang, D. *Angew. Chem., Int. Ed.* **2011**, *50*, 2738−2741.

(10) Zhong, J. Y.; Cao, C. B.; Liu, Y. Y.; Li, Y. A.; Khan, W. S. *Chem. Commun.* **2010**, *46*, 3869−3871.

(11) Yin, X. M.; Li, C. C.; Zhang, M.; Hao, Q. Y.; Liu, S.; Li, Q. H.; Chen, L. B.; Wang, T. H. *Nanotechnology* **2009**, *20*, 455503.

(12) Choi, K. I.; Kim, H. R.; Lee, J. H. *Sens. Actuators, B* **2009**, *138*, 497−503.

(13) Guo, Z.; Liu, J. Y.; Jia, Y.; Chen, X.; Meng, F. L.; Li, M. Q.; Liu, J. H. *Nanotechnology* **2008**, *19*, 345704.

(14) Zhang, J.; Wang, S. R.; Wang, Y.; Xu, M. J.; Xia, H. J.; Zhang, S. M.; Huang, W. P.; Guo, X. Z.; Wu, S. H. *Sens. Actuators, B* **2009**, *139*, 411−417.

(15) Sakai, G.; Matsunaga, N.; Shimanoe, K.; Yamazoe, N. *Sens. Actuators, B* **2001**, *80*, 125−131.

(16) (a) Kawasashi, N.; Matijevíc, E. *J. Colloid Interface Sci.* **1991**, *143*, 103−110. (b) Lee, J. Y.; Lee, J. H.; Hong, S. H.; Lee, Y. K.; Choi, J. Y. *J. Mater. Res.* **2004**, *19*, 1669−1675. (c) Hieda, K.; Hyodo, T.; Shimizu, Y.; Egashira, M. *Sens. Actuators, B* **2008**, *133*, 144−150.

(17) Lee, J. H. *Sens. Actuators, B* **2009**, *140*, 319−336.

(18) He, L. F.; Jia, Y.; Meng, F. L.; Li, M. Q.; Liu, J. H. *J. Mater. Sci.* **2009**, *44*, 4326−4333.

(19) Sun, Z. Y.; Yuan, H. Q.; Liu, Z. M.; Han, B. X.; Zhang, X. R. *Adv. Mater.* **2005**, *17*, 2993−2996.

(20) Liu, J. H.; Huang, X. J.; Ye, G.; Liu, W.; Jiao, Z.; Chao, W. L.; Zhou, Z. B.; Yu, Z. L. *Sensors* **2003**, *3*, 110−118.

(21) Liao, L.; Lu, H. B.; Li, J. C.; Liu, C.; Fu, D. J.; Liu, Y. L. *Appl. Phys. Lett.* **2007**, *91*, 173110.

(22) Rout, C. S.; Hegde, M.; Rao, C. N. R. *Sens. Actuators, B* **2008**, *128*, 488−493.

(23) Rakhshani, A. E. *Solid-State Electron.* **1986**, *29*, 7−17.

(24) Liu, B.; Zeng, H. C. *J. Am. Chem. Soc.* **2004**, *126*, 8124−8125.

(25) Gao, S. Y.; Yang, S. X.; Shu, J.; Zhang, S. X.; Li, Z. D.; Jiang, K. *J. Phys. Chem. C* **2008**, *112*, 19324−19328.

(26) Guan, X. F.; Li, G. L. P.; Li, S.; Fu, Z. W.; Zheng, J.; Yan, T. J. *J. Alloys Compd.* **2011**, *509*, 3367−3374.

(27) Yang, S. Y.; Wang, C. F.; Chen, L.; Chen, S. *Mater. Chem. Phys.* **2010**, *120*, 296−301.

(28) Deng, C. H.; Hu, H. M.; Ge, X. Q.; Han, C. L.; Zhao, D. F.; Shao, G. Q. *Ultrason. Sonochem.* **2011**, *18*, 932−937.

(29) Manna, S.; Das, K.; De, S. K. *ACS Appl. Mater. Interfaces* **2010**, *2*, 1536−1542.

(30) Zhang, F.; Zhu, A. W.; Luo, Y. P.; Tian, Y.; Yang, J. H.; Qin, Y. *J. Phys. Chem. C* **2010**, *114*, 19214−19219.

(31) Lu, C. H.; Qi, L. M.; Yang, J. H.; Zhang, D. Y.; Wu, N. Z.; Ma, J. M. *J. Phys. Chem. B* **2004**, *108*, 17825−17831.

(32) (a) Penn, R. L.; Banfield, J. F. *Science* **1998**, *281*, 969−971. (b) Liu, C. M.; Yang, S. H. *ACS Nano* **2009**, *3*, 1025−1031.

(33) Moulder, J. F.; Stickle, W. F.; Sobol, P. E.; Bomben, K. D. *Handbook of X-ray Photoelectron Spectroscopy*; Perkin−Elmer: Eden Prairie, MN, 1992.

(34) Lou, X. W.; Wang, Y.; Yuan, C. L.; Lee, J. Y.; Archer, L. A. *Adv. Mater.* **2006**, *18*, 2325−2329.

(35) Yang, H. G.; Zeng, H. C. *J. Phys. Chem. B* **2004**, *108*, 3492−3495.

(36) Zhang, X. J.; Wang, G. F.; Liu, X. W.; Wu, J. J.; Li, M.; Gu, J.; Liu, H.; Fang, B. *J. Phys. Chem. C* **2008**, *112*, 16845−16849.

(37) Chen, J.; Wang, K.; Hartman, L.; Zhou, W. *J. Phys. Chem. C* **2008**, *112*, 16017−16021.

(38) Tu, J.; Li, N.; Lai, X.; Chi, Y.; Zhang, Y.; Wang, W.; Li, X.; Li, J.; Qiu, S. *Appl. Surf. Sci.* **2010**, *256*, 5051−5055.

(39) Kaur, M.; Jain, N.; Sharma, K.; Bhattacharya, S.; Roy, M.; Tyagi, A. K.; Gupta, S. K.; Yakhmi, J. N. *Sens. Actuators, B* **2008**, *133*, 456−461.

12000

dx.doi.org/10.1021/jp212029n | *J. Phys. Chem. C* 2012, 116, 11994−12000